

Cite this: *J. Mater. Chem. A*, 2024, **12**, 2839

# An intrinsically zwitter-ionic COF: a carboxylic acid and pseudo-tetrahedral $sp^3$ nitrogen functionalized covalent organic framework with potential for humidity sensing†

Shyamapada Nandi,<sup>†</sup> Himan Dev Singh,<sup>‡</sup> Pragalb Shekhar,<sup>b</sup> Debanjan Chakraborty,<sup>b</sup> Rinku Kushwaha<sup>b</sup> and Ramanathan Vaidhyanathan<sup>\*bc</sup>

Herein, we report a zwitter-ionic covalent organic framework (COF) simultaneously functionalized with carboxylic acid and protonatable  $sp^3$  nitrogen. The acidity and basicity of these functional groups are so well balanced that they can be easily protonated and deprotonated by using water/humidity. Color changes visibly display the dry and wet states. We believe that in the presence of moisture, it becomes zwitter-ionic, with the carboxylic acid getting deprotonated and concertedly protonating the  $sp^3$  nitrogen centers. This directly impacts the extent of conjugation in the carboxylate group carrying module of the COF, triggering the color change. This was corroborated by a lack of color change under humid conditions when a structurally equivalent COF devoid of carboxylic acid groups was employed. The pseudo-tetrahedral  $sp^3$  nitrogen centers and the freely rotatable bulky carboxylic acid group in the framework's backbone weaken the  $\pi$ -stacking between the COF layers; this allows the COF to exfoliate into nanosheets with ease. The organic dispersions of these nanosheets are highly luminescent under UV radiation. A trace quantity of water in the organic solvent completely quenches the luminescence, enabling the COF to act as a moisture sensor for organic solvents with a very impressive detection limit (LOD = 0.027% in acetonitrile; LOD = 0.128% in acetone). A Gaussian calculation reveals an alteration in the frontier orbitals of the zwitterionic vs. acid forms. DFT and MD modeling studies reveal that though the water's interaction with the COF is not strong, it is kinetically favored, which is important in reversible protonation–deprotonation chemistry. Thus, this designer COF represents an applicable solid-state humidity/water sensing material.

Received 6th September 2023  
Accepted 13th November 2023

DOI: 10.1039/d3ta05416k

rsc.li/materials-a

## Introduction

Controlling humidity is an important target in several sectors, such as automobiles, indoor-air-management, battery-production, pharmaceutical and food industries, and chemical and biological reactions.<sup>1–6</sup> For example, it is necessary to control the humidity (relative humidity of 40–60% according to the US Environmental Protection Agency) of an indoor environment where people spend a substantial amount of time daily.<sup>7</sup> Besides our daily life, humidity plays a major role in several chemical/biological

processes.<sup>8–11</sup> In many cases, the reactions work only under inert and moisture-free conditions.<sup>12,13</sup> Also, the yields and the purity of the products formed can be very sensitive to the amount of moisture in the reaction/solvents. It plays a critical role in organometallic chemistry where traces of water in the solvent can lead to explosion and fire accidents.<sup>14</sup> The presence of moisture in petroleum-based fuels can compromise the performance and life of the engines due to clogged fuel channels at low temperatures. The use of humidity sensors in such cases becomes inevitable. In the automotive industry, these humidity sensors are used in rear window defoggers and motor assembly lines; in the pharmaceutical industry, they are used in respiratory equipment,<sup>15</sup> sterilizers, incubators,<sup>16</sup> pharmaceutical processing<sup>2</sup> and biological products;<sup>16</sup> in the food processing industry,<sup>2</sup> they find application in dryers, ovens, film desiccation, and paper and textile production.<sup>17</sup> This is why there is an ever-growing demand for humidity sensors in every sector, including our daily lives.

In this regard, porous crystalline materials can be very efficient in humidity sensing and humidity control depending on

<sup>a</sup>Chemistry Division, School of Advanced Sciences, Vellore Institute of Technology, 600127, Chennai, India. E-mail: shyamapada.nandi@vit.ac.in

<sup>b</sup>Department of Chemistry, Indian Institute of Science Education and Research, 411008, Pune, India

<sup>c</sup>Centre for Energy Science, Indian Institute of Science Education and Research, 411008, Pune, India. E-mail: vaidhya@iiserpune.ac.in

† Electronic supplementary information (ESI) available. See DOI: <https://doi.org/10.1039/d3ta05416k>

‡ These authors contributed equally.

the pore size and different functionalities incorporated into the structure by design.<sup>18–20</sup> Covalent organic frameworks are a relatively new class of metal-free crystalline, ordered and porous polymers that have gained significant interest in the past decade for various applications such as gas separation and storage,<sup>21–24</sup> biomedical applications,<sup>25</sup> charge storage,<sup>26–29</sup> heterogeneous catalysis,<sup>30–36</sup> photocatalysis,<sup>37–39</sup> optics,<sup>40–42</sup> sensing,<sup>43–50</sup> and bioimaging.<sup>51</sup> Recently, different functionalized COFs have found use in sensing such as pH sensing,<sup>52,53</sup> HCl/acidic vapor sensing,<sup>44,45</sup> water contaminant sensing,<sup>47</sup> *etc.* In addition to these applications, these novel materials have started to gain interest in humidity/water sensing applications.<sup>19,54–56</sup> For instance, Auras and coworkers have reported a pyrene-based COF showing color shifts on exposure to water and other volatile solvent vapors.<sup>49</sup> This COF shows a very good response time for humidity sensing, but the change in the absorption spectrum is very small (the shift is 20–30 nm) upon exposure to humidity. Marder and co-workers reported humidity sensing in covalent organic frameworks through a reversible isomerization in an imine-based COF.<sup>54</sup> This COF system also shows a rapid response with the color change visible to the naked eye. Kaskel and co-workers recently reported chemically stable carbazole-based COFs for humidity control applications.<sup>48</sup> However, these COFs are developed from ligands that need to be synthesized in multistep reactions, making these COFs quite expensive. The COFs made from relatively simple linkers would be a better candidate for sensing-type applications. Also, finding new chemical principles governing such humidity-triggered color changes adds immense value. In this work, we have developed a novel –COOH functionalized COF from simple and cheap linkers that shows a dramatic color change (visible to the naked eye) on exposure to moisture. When dispersed in different organic solvents, this COF shows a photoluminescent character upon excitation with UV radiation. We have further utilized this COF's property for sensing water traces in various organic solvents such as acetone, acetonitrile (ACN), *etc.* The dramatic color change of the framework was attributed to its water-induced protonation/deprotonation. DFT/Gaussian-based molecular simulations further supported this.

## Results and discussion

### Synthesis of IISERP-COF31 (1)

The tripodal aldehyde, tris[4-formylphenyl] amine and dipodal amine (with an angle of 120° between the two –NH<sub>2</sub> groups) 3,5-diaminobenzoic acid were employed to synthesize the Schiff bonded COF bearing sp<sup>3</sup> nitrogen and a free –COOH group in it. A typical synthesis was carried out solvothermally *via* the condensation of the aldehyde and the amine in a mixture of mesitylene, *o*-dichlorobenzene and ethanol at 120 °C for 72 hours (Fig. 1A and Scheme S1†). The solvothermal reaction produces an orange-yellow powder, which was washed thoroughly with ethanol. This powder was further subjected to routine characterization such as powder XRD diffraction, thermogravimetric analysis (TGA), porosity analysis, FTIR and solid-state NMR spectroscopy. Strikingly, this COF turns bright red on

exposure to the atmosphere (humidity); the original orange color is regained if the sample is dried. To obtain a good PXRD pattern, we used the wet sample, which was directly collected from the synthesis tube with a small amount of the solvents to avoid exposure to atmospheric humidity.

### Structure solution

A two-dimensional (2D) structure consisting of puckered hexagonal layers in agreement with the experimentally observed powder X-ray pattern of IISERP-COF31 (1) was modelled using the Material Studio program (Fig. 1B, S1–S3†). We followed a similar technique for the structure solution as that presented in our earlier studies.<sup>35,57</sup> Accordingly, PXRD was indexed using the XCELL program to identify a suitable space group (P1 (FOM: >20)). Following this, the model was constructed in a triclinic cell. The presence of asymmetrically placed carboxylic acid and an sp<sup>3</sup> nitrogen moiety tends to such low symmetry. This structure was geometry optimized using a tight-binding density functional theory (DFTB) algorithm embedded in the Materials Studio program. In the optimized geometry, the structure adopts a P1 space group. A Pawley refinement of the powder pattern against the modeled cell was performed to generate the final structure ( $a = 18.2534 \text{ \AA}$ ;  $b = 31.6061 \text{ \AA}$ ;  $c = 32.1046 \text{ \AA}$ ;  $\alpha = 118.47^\circ$ ,  $\beta = 90.87^\circ$ ,  $\gamma = 89.17^\circ$ ;  $R_p = 4.20$  and  $wR_p = 5.58$ ). Unlike normal hexagonal 2D COFs, the layers of this COF are buckled because of the presence of sp<sup>3</sup> nitrogen centers in the aldehyde core.<sup>58</sup> The framework could be solved equally well for eclipsed as well as staggered geometry (Fig. 2, S2 and S4†). Hence, we rationalized the potential structure of the COF *via* experimental porosity (Fig. 2C and D). Note: the porosity for every phase was established using multiple batches of samples and from different instruments (Micromeritics ASAP 2020 and 3-flex). The structure wherein the layers are organized with an eclipsed configuration would have had a large pore size of  $29.1 \times 26.7 \text{ \AA}$  (Fig. S1†), which is not the case. The staggered lattice with a pore size of  $13.0 \text{ \AA}$  (Fig. 1B) gives a good Pawley fit and agrees well with the experimentally determined pore sizes. Due to the propeller-like configuration around the sp<sup>3</sup> nitrogen, the flat layers are not favored; instead, distinctly buckled layers are formed, and they slipped over each other to give an ABAB... type stacking (Fig. 1C). This gives the framework a pseudo-3D structure, and the layers are held together rather weak van der Waals and hydrogen-bond type interactions, unlike the archetypal flat layers found in COFs constructed from pi-stacking of planar building units.

### Bulk characterization

The solid product of the solvothermal reaction was first characterized by powder X-ray diffraction (PXRD). The as-made wet sample shows an intense low angle peak ( $2\theta = 6.25^\circ$ ) and several other peaks, which are indexed based on the crystalline model, confirming the successful synthesis of a crystalline material (Fig. 2A).

However, exposing 1 to the atmosphere followed by heating it in an oven at 90 °C shows an increase in the intensity of peaks at  $2\theta = 18^\circ$  and  $23^\circ$  corresponding to the interlayer spacing

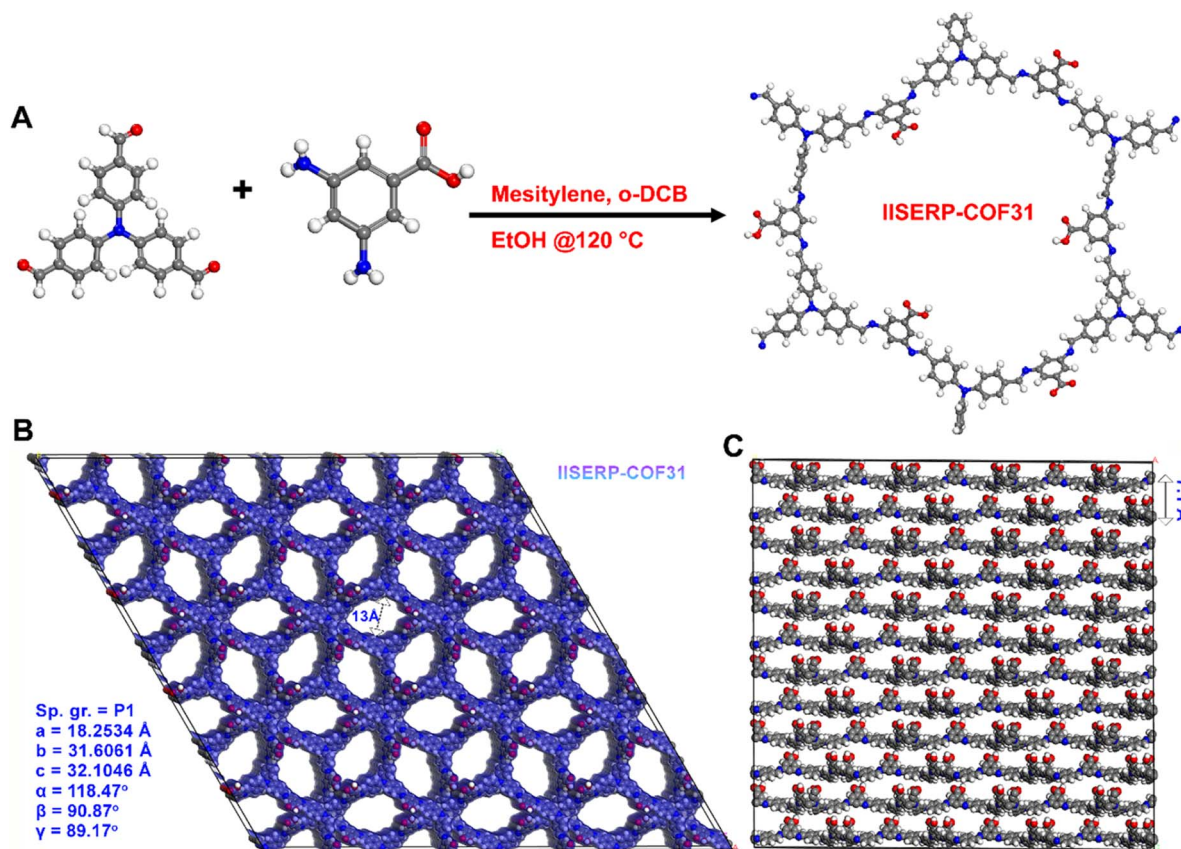


**Fig. 1** (A) A schematic diagram of the COOH functionalized COF (**1**) with synthetic details. Note: the polymerized structure is just a ChemDraw representation to indicate the framework connectivity and not the solved structure. (B) Connolly representation (probe radius: 1.4 Å) of the DFT-optimized structure of **1** showing the small pores. (C) The layer stacking of **1**. The carboxylic acid moieties protrude into the interlayer spaces. Color code: C – grey, N – blue, O – Red, and H – White.

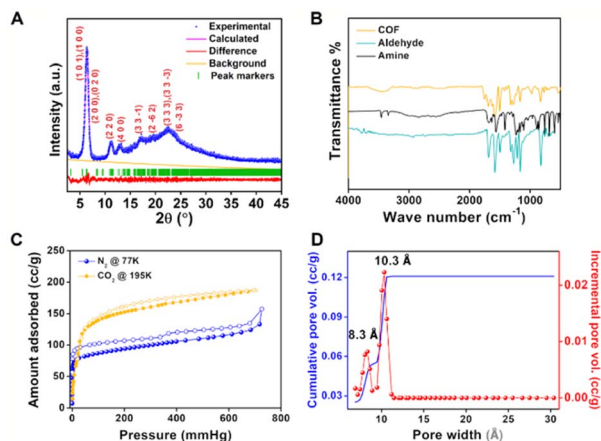


**Fig. 2** (A) The fit obtained from Pawley refinement of **1**. Final refinement parameters,  $R_p = 4.20$  and  $wR_p = 5.58$ . (B) FTIR spectra of **1** compared with that of the starting monomers, aldehyde and the amine. The spectrum of **1** shows the presence of free  $-\text{COOH}$  groups. (C)  $\text{N}_2$  (77 K) and  $\text{CO}_2$  (195 K) isotherms of **1** showing the microporous nature of the COF. (D) Pore size distribution plot of **1** calculated from the 77 K  $\text{N}_2$  isotherm using the NLDFT model.

related reflections, which hints towards the possible disruption of the layer stacking (Fig. S5<sup>†</sup>). As the structure modeling suggests, weakly  $\pi$ -stacked layers are present in the framework, which a gentle external stimulus can easily exfoliate. The COF powder was exposed to air and heated at higher temperatures under vacuum to achieve further exfoliation. The heated samples showed a further increase in the intensity of the interlayer spacing related reflections expected with the exfoliation of the COF (Fig. S5<sup>†</sup>). Hence, it was realized that the exfoliated material has a more thermodynamically favorable phase than the as-made COF. Therefore, all the measurements and experiments (unless mentioned) in this study were conducted on exfoliated covalent organic nanosheets (CONs).

Thermogravimetry analysis of **1** shows that the framework maintains its integrity up to a temperature of 350 °C (Fig. S6<sup>†</sup>), which confirms that the intensity changes in the PXRD pattern of samples heated at lower temperatures are not due to the breakdown of the covalent bonds present in the COF layers. Fourier transform infrared (FTIR) spectra of **1** suggest the absence of peaks corresponding to the diamine group, which indicates the full consumption of  $\text{NH}_2$  groups of monomers. A typical vibration band due to  $\text{C}=\text{N}$  at  $1586\text{ cm}^{-1}$  was observed along with the other bands ( $\text{C}=\text{O}$ ,  $1753\text{ cm}^{-1}$  and  $\text{O}-\text{H}$ ,

3448  $\text{cm}^{-1}$ ) corresponding to the framework. The bands corresponding to C=O and O–H confirm the integrity of the –COOH group in the framework unambiguously (Fig. 2B). The formation of Schiff bonds was further confirmed by solid-state  $^{13}\text{C}$  magic angle spinning NMR spectra, which show a peak at  $\delta = 155$  ppm. Also, the peak corresponding to the carboxylic group could be observed from the  $^{13}\text{C}$  NMR spectrum (Fig. S7†). The permanent porosity of **1** has been established by using  $\text{N}_2$  and  $\text{CO}_2$  adsorption at 77 K and 195 K, respectively. The  $\text{N}_2$  adsorption at 77 K shows a Type I isotherm, a characteristic of a microporous material, with a saturation uptake of  $120 \text{ cm}^3 \text{ g}^{-1}$  (Fig. 2C). A non-local density functional theory (NLDFT) fit to the adsorption branch of the nitrogen isotherm yields a major pore size of 10.3 Å and 8.3 Å, which matches the structure (Fig. 2D). The Brunauer–Emmett–Teller (BET) and Langmuir surface areas were estimated to be 340 and  $520 \text{ m}^2 \text{ g}^{-1}$ , respectively (Fig. S8†). Similarly,  $\text{CO}_2$  shows a type I isotherm (at 195 K) with higher uptake than  $\text{N}_2$  (Fig. 2). The morphological studies of **1** were conducted using field emission scanning electron microscopy (FE-SEM). **1** has a cotton-ball-like morphology with small spikes (Fig. 3A, S9 and S10†). These spikes are the small nano-crystallites of **1**, and these crystallites have aggregated to form a cotton ball-like structure. Furthermore, it could be observed from the high-resolution transmission electron microscopy (HRTEM) images that these cotton balls are made up of aggregated flakes (Fig. 3B and S11†). It is worth mentioning that we could observe the lattice fringes in

the HRTEM images (Fig. S11†) indicating the high degree of crystallinity of the material.

As mentioned, **1** can be easily exfoliated *via* exposure to the atmosphere, followed by thermal treatment. Due to this exfoliation, the number of  $\pi$ -stacked layers decreases and results in the formation of nanosheets, which contain very few  $\pi$ -stacked layers. In this case, atomic force microscopy (AFM) was used to probe the thickness of the nanosheets. The images taken by AFM showed the formation of covalent organic nanosheets (CONs) with an average thickness of  $\sim 4\text{--}6$  nm (Fig. 3C, D and S12†). The Tyndall effect also confirmed the formation of nanosheets. **1** was soaked in different solvents in glass vials and sonicated for 10 minutes; after this, laser light was shed onto these vials from one end at regular intervals. The path of light through the solution could be traced even when it is kept undisturbed for 6 hours, which implies that the dispersed material didn't settle down upon standing for a long time. This again proves the colloidal stability of nanosheets in the solutions (Fig. 3 and S13†). The average size of the nanosheets was found to be between 500 and 600 nm, as confirmed by the dynamic light scattering (DLS) experiments performed on the exfoliated COF across three different batches (Fig. S14†). The easy exfoliation of **1** is in good agreement with our previous observation, where an imine bonded COF constructed from a 3,5-diamino-1,2,4-triazole (the angle between the two  $\text{NH}_2$  group is close to  $120^\circ$ ) was found to be self-exfoliated during the synthesis itself.<sup>59</sup>

### Optical studies

Impressed by the drastic color change of **1** from yellow to bright red upon exposure to air, we recorded solid-state UV-vis spectra for both the samples, dry (yellow) and humidified (red) (Fig. 4A). The dry one gives absorption maxima at 447 nm, whereas the humidity-exposed sample shows absorption maxima at 362 nm (Fig. 4B). The direct optical band gap was calculated from the Tauc plot, and it was found that the band gap increases from 2.27 eV to 2.87 eV when the color of the sample changes from yellow to bright red (Fig. 4C). We stored the sample under vacuum to trace the stimuli for the color change. Dry nitrogen and oxygen were passed over the sample (since  $\text{N}_2$  and  $\text{O}_2$  are major gases in the atmosphere) in two different experiments, but no change in the color of **1** was observed. Then, in a separate investigation, humid nitrogen and humid  $\text{O}_2$  were passed over the sample in a similar fashion, resulting in the sample's immediate color change from orange-yellow to red in both experiments. Hence, this set of four experiments concluded that humidity is responsible for the color change, which is independent of the nature of the carrier gas.

The mechanism of the visible color change of the nanosheets was attributed to the water-induced protonation and deprotonation of the framework. For the dry sample, when there is no moisture in the system, the –COOH group of the framework is in the neutral form (Fig. S15†). As soon as moisture is introduced into the system, the framework converts to the zwitterionic form, where the  $\text{sp}^3$  nitrogen of aldehyde is protonated and the –COOH group is deprotonated (Fig. 4D and S16†). This

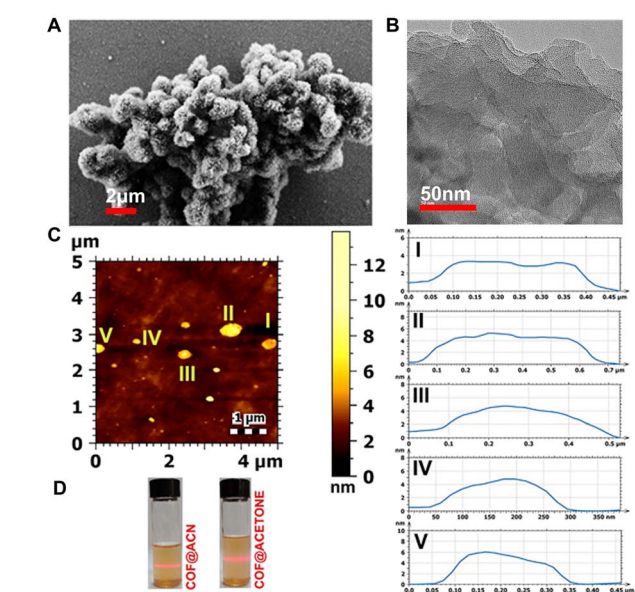


Fig. 3 (A) FESEM image of **1** showing the cotton-ball like morphology with small spikes on it. (B) HRTEM image of **1** showing a flake kind of structure. The inset showing the lattice fringes having an inter planar distance of 0.26 nm which is very close to the interlayer distance obtained from the structural model. (C) (Top) AFM image of **1** showing its nanosheet character. (Bottom) **1** dispersed in different solvents showing the Tyndall effect for a prolonged time. (D) The height profile plot shows the thickness of the nanosheets to be in the range of  $\approx 4\text{--}6$  nm (see the ESI† for more images).

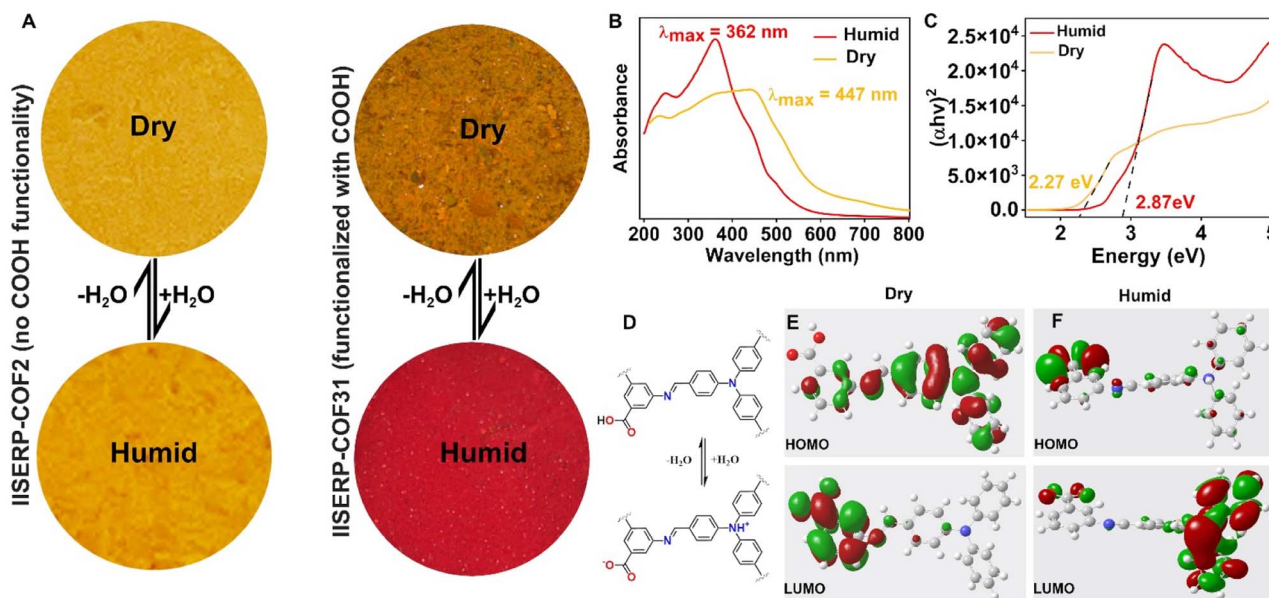


Fig. 4 (A) A comparative photographic image of **1** and IISRRP-COF2 under dry and humid conditions showing the visible colour change only in the case of **1**. (B) Solid state UV-vis spectra of **1** under dry and humid conditions showing the change in  $\lambda_{\text{max}}$  of the absorption spectra. (C) Tauc plot showing the direct bandgap derived from the UV-vis spectra. Note: the change in the bandgap upon humidity exposure is in good agreement with the visible color change of **1**. (D) Schematic diagram showing the possible mechanism for the visible color change of **1**. (E) The frontier orbitals of the model compound in the dry state derived from a DFT/Gaussian calculation. (F) The frontier orbitals of the model compound under humid conditions derived from a DFT/Gaussian calculation.

COO<sup>-</sup> thus generated by humidity or water can supply more electrons into the conjugated system. This phenomenon is accountable for altering the frontier orbitals (HOMO and LUMO) of **1**, and thereby responsible for the color change. Therefore, the simultaneous presence of the sp<sup>3</sup> nitrogen and the free terminal COOH group in the framework is necessary to observe such a humidity-dependent color change. This was further proved by synthesizing a COF (IISERP-COF2)<sup>58</sup> where the sp<sup>3</sup> nitrogen is present but the -COOH group is absent. As expected, this COF shows no humidity-dependent color change (Fig. 4A and S17<sup>†</sup>). The role of water/protonated water is crucial to impart this effect. The XPS spectra of **1** (after exposure to atmospheric humidity) further support this protonation. As presented in Fig. S18,<sup>†</sup> the N1s spectrum shows a quaternary nitrogen site in **1**, indicating the protonation of the sp<sup>3</sup> nitrogen present in the framework. However, in the XPS spectra of IISERP-COF2 we did not observe any quaternary nitrogen.<sup>58</sup>

To shed more light on the mechanism of the visible color change, we resorted to DFT/Gaussian-based simulations. For this, we have created the smallest possible model compounds for dry and humid conditions, as presented in Fig. 4D. These model compounds were first geometry optimized using a DFT method embedded in Materials Studio. The optimized model compounds were then used for the Gaussian calculation using density functional theory based on the B3LYP hybrid functional method with the 6-311G basis set.<sup>60,61</sup> The extracted frontier orbitals clearly show that in the case of dry conditions, the HOMO is located around the triphenylamine core of the aldehyde unit and the LUMO is located around the free -COOH group and the phenyl ring of amine (Fig. 4E). However, under

humid conditions when **1** exists in the zwitterionic form, the HOMO is located around the -COO<sup>-</sup> group and the LUMO is located around the triphenylamine core of the aldehyde part (Fig. 4F). This switching of the HOMO and LUMO between the dry and the humid model is responsible for the dramatic visual color change.

Another important feature of **1** is its photoluminescent character. **1** dispersed in different organic solvents emits blue light upon excitation with UV radiation. However, the presence of water in the organic solvents quenches the luminescence. We have utilized this property of **1** for sensing trace amounts of water in different organic solvents. We first recorded the photoluminescence (PL) spectra of **1** in different solvents such as acetone, tetrahydrofuran (THF), dimethyl formamide (DMF), dimethyl acetamide (DMA), methanol (MeOH), ethanol (EtOH), dimethyl carbonate (DMC), acetonitrile (ACN), *etc* at 30 °C (Fig. S19<sup>†</sup>). The emission occurs at ~455–480 nm for all the verified solvents. However, the PL intensity was different for each solvent. To study the sensing of trace water in organic solvents, we chose two solvents, ACN and acetone. A small amount of **1** (5 mg) was dispersed in 2 ml of the respective solvents, and PL spectra were recorded. Then, deionized water (2  $\mu\text{L}$  to 250  $\mu\text{L}$ ) was added sequentially to the cuvette, and PL spectra were recorded after every addition of water. It was observed that even with the addition of a very small amount of water (2  $\mu\text{L}$ ), a remarkable change in the intensity of the peak in the PL emission spectra was observed. This quenching of the emission increases with further addition of water (Fig. 5A and B). This decay in emission with the addition of miniscule amounts of water shows the sensitivity of **1** towards moisture. In

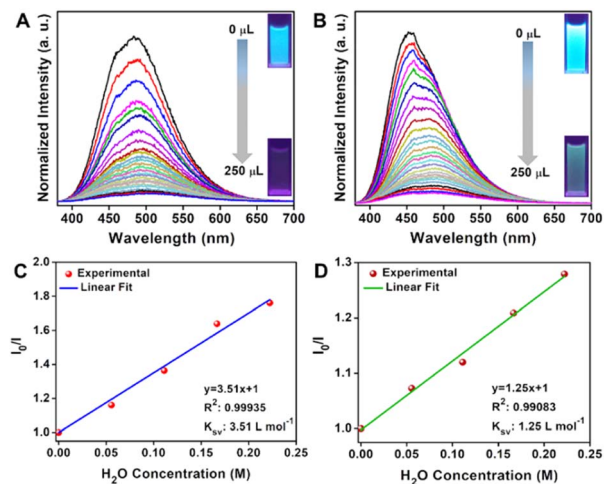


Fig. 5 (A) PL spectra of **1** dispersed in ACN showing the quenching of photoluminescence upon gradual addition of water (B) PL spectra of **1** dispersed in acetone showing the quenching of photoluminescence upon gradual addition of water (C) A Stern–Volmer plot at a low water concentration in ACN showing the linearity. (D) A Stern–Volmer plot at a low water concentration in acetone showing the linearity.

both the solvents, the fluorescence intensity decays very fast initially and then tends to slow down (Fig. S20 and S21†). Nearly 80% of the fluorescence intensity is quenched by adding 1 vol% of water. The detection limit was calculated from a linear fit to the fluorescence intensity vs. water concentration (in the low-concentration region) graph. The limit of detection (LOD) was 0.027% and 0.128% in the case of ACN and acetone, respectively (Fig. S20 and S21†). It is worth mentioning that the LOD values are better or comparable to those of some of the best-known COFs/MOFs/carbon materials for water sensing (Table S1†). Notably, the sensing works the best in acetonitrile (ACN), in which the emission peak shows a sharp decrease in intensity with the addition of just 2  $\mu$ L of water. This PL intensity becomes zero when the water content is increased to 250  $\mu$ L. However, in the case of acetone, a decrease in the PL intensity of the emission peak is observed with successive addition of water, but it doesn't decay to zero with the same amount of water. The same observation can be visualized in the optical images, which show complete switch ON and OFF sensing in the case of acetonitrile; however, in the case of acetone, the effect is not so prominent (Fig. 5). This could be due to the higher polarity of ACN ( $\epsilon = 37.5$ ) compared to that of acetone ( $\epsilon = 20.7$ ). Furthermore, a Stern–Volmer plot in the low water content region shows linear behavior in both cases (Fig. 5C and D), indicating a strong water interaction with **1** dispersed in ACN or acetone.<sup>62</sup> The Stern–Volmer coefficient was calculated to be 3.51  $L mol^{-1}$  and 1.25  $L mol^{-1}$  for the case of ACN and acetone, respectively. The sensing of a trace amount of water in organic solvents using **1** is highly reproducible (Fig. S22 and S23†). It is important to mention that the material can be recovered after the 1st cycle by drying under vacuum, and the dried material can be used in the next cycle (Fig. S24†). The recyclability of the material was attributed to its good water stability, which was confirmed by the PXRD and FTIR study of the water-soaked

sample (Fig. S25†). The humidity sensing by **1** was established in the solid state as well. The color of the as-made COF (orange-yellow) changes to bright red upon adding a drop of water to it (Fig. S26†). Also, this change is reversible, *i.e.*, the color changes to yellow upon drying the COF in a vacuum. This color change is fully reversible and can be achieved for multiple cycles. Though these studies indicate that water in the vapor form strongly interacts with the COF, the water adsorption isotherm suggests the opposite (Fig. S27†). We set out to address this incongruity.

### Interaction of water and protonated water with the COF

Considering the COF's immediate color response to even vapor phase water (humidity), one would expect an abrupt water uptake at low partial pressures in an isotherm. Against this expectation, the water isotherm was shallow with a nominal saturation capacity. To further verify this, we calculated the isosteric heat for a single water molecule as well as a protonated water molecule inside the COF in Henry's regime. It was very low ( $<10 kcal mol^{-1}$ ), which agrees well with the shallow low-pressure uptake observed from experimental isotherms. This suggests that sensing is not due to physisorptive uptake of water by the material. If we consider the alternative, proton abstraction from COF's functional groups by water, it would be expected to be a lot more sensitive and efficient even at low water concentrations, which seems to be the case. Now, we realize that this water could be playing a key role in transferring the acidic proton present on the free carboxylic acid in the framework to these lone-pair containing  $sp^3$  nitrogen centers, giving rise to the zwitter-ionic form with a markedly different color. To verify this, we attempted to identify the most-favorable position for  $H_3O^+$  in the COF, which again turned out to be the same space occupied by neutral water (Note: one of the carboxylic acid groups was converted to carboxylate during the introduction of  $H_3O^+$ ) (Fig. 6).

The color change on the COF flake is quite rapid with the introduction of humidity (low water concentration); this is likely to be a diffusion-controlled kinetic process. Hence, we wanted to know how favorable it is for protonated water molecules to diffuse into the pores. This is extremely difficult to determine experimentally; therefore, we resorted to molecular dynamics. The optimized structure was equilibrated using an NPT ensemble, and the average lattice parameters were employed for the output structure. The migration of protonated water/neutral water in the cationic framework was explored under the NVT conditions. The final trajectory was obtained from a 50 ns microcanonical NVE dynamics performed at 300 K. The mean square displacement (MSD) vs. time plots were used to calculate the average diffusion coefficient for the guest species (Fig. 6F). Importantly, the diffusion coefficient for the single protonated water molecule per unit cell is  $7.16 \times 10^{-6} cm^2 s^{-1}$ ; while that of neutral water is  $8.9 \times 10^{-6} cm^2 s^{-1}$ , and for six protonated water molecules per unit cell, it is  $3.54 \times 10^{-4} cm^2 s^{-1}$ . These are extremely favorable, and such high values support the rapid sensing of humidity by the COF material. The build-up of more and more protonated water improves their self-diffusion, most likely through cooperativity. Also, these high diffusion values suggest that this humidity sensing is not a mere surface

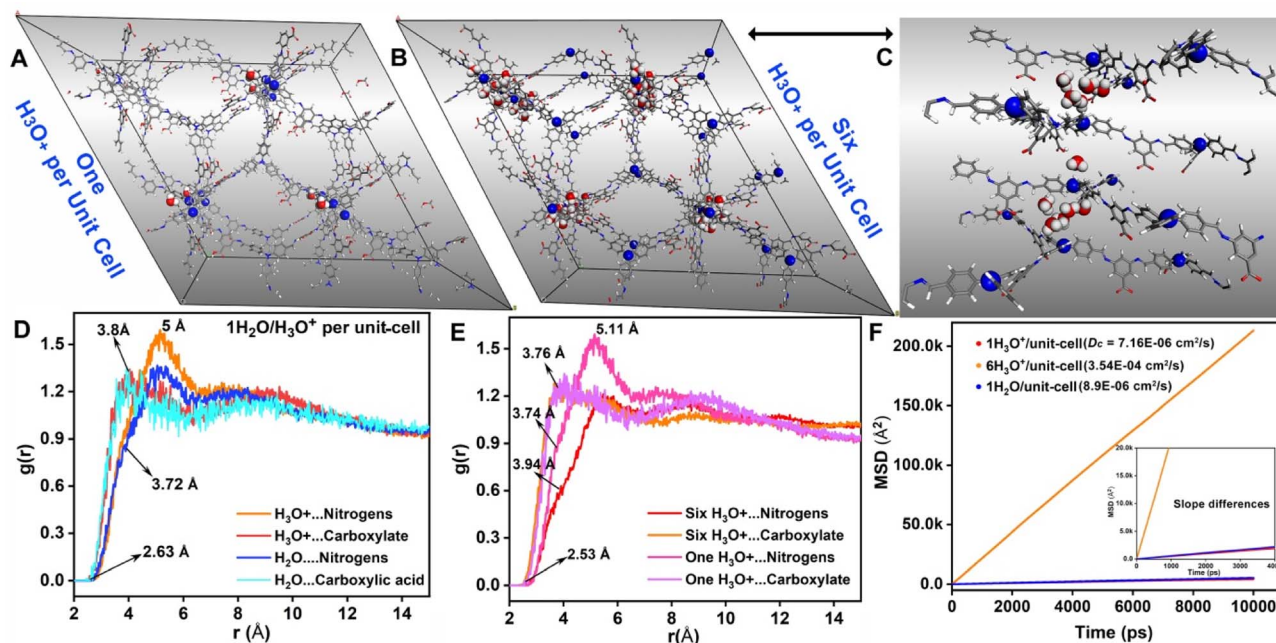


Fig. 6 (A) A DFT-optimized structure of H<sub>3</sub>O<sup>+</sup> in a COF with a loading of 1H<sub>3</sub>O<sup>+</sup>/unit-cell. sp<sup>3</sup> nitrogen and protonated water sandwiched between them are shown in balls. (B) and (C) DFT-optimized structure of 6H<sub>3</sub>O<sup>+</sup>/unit-cell in 1 showing the protonated water sandwiched by the sp<sup>3</sup> nitrogen from two different layers. (D) and (E) The RDF plots from MD simulations of 1 with 1H<sub>3</sub>O<sup>+</sup> and 6H<sub>3</sub>O<sup>+</sup>/unit-cell displaying the distances between the protonatable sites (donor) and the water molecules (acceptor). (F) The mean square displacement vs. time plot from MD simulations showing favourable diffusion for both neutral and protonated water inside the COF, and with high H<sub>3</sub>O<sup>+</sup> concentration, the diffusion coefficient increases drastically.

phenomenon but a diffusion-controlled process. Importantly, a broader insight is developed: for solid-state sensing, one need not have strong equilibrium interactions between the guest and the host; rapid diffusion-controlled kinetics is the key.

## Conclusion

In conclusion, we have developed for the first-time a –COOH functionalized and sp<sup>3</sup> N rich imine bonded COF which can be easily exfoliated to nanosheets of a few nm thickness. This COF reversibly changes its color from orange-yellow to bright red when exposed to humidity. This dramatic color change could be used for developing potential humidity sensors. We attributed this color change to the humidity dependent protonation or deprotonation of the tertiary amine and free –COOH group present in the framework. This was further supported by the DFT/Gaussian based calculations. Furthermore, the nanosheets dispersed in organic solvents emit blue light upon excitation with UV radiation. This luminescence is completely quenched upon addition of a small quantity of water. This property of the COF has been utilized for detection of trace quantity of water in different organic solvents. This study would help in designing next generation COF based humidity sensors.

## Experimental

### Synthesis of IISERP-COF31

Tris[4-formylphenyl]amine (0.25 mmol) and 3,5-diaminobenzoic acid (0.37 mmol) were added in a Pyrex tube and

dissolved in 2 ml mesitylene, 3 ml o-dichlorobenzene and 4 ml ethanol. 0.25 ml acetic acid was added to this mixture and was stirred well. The Pyrex tube was then flash frozen using liquid nitrogen and sealed. The contents in the sealed tube were heated at 120 °C for 3 days. After cooling to room temperature, the light-yellow precipitate was filtered and washed with DMF, THF, and MeOH. The isolated yield was 76% with respect to the aldehyde. The solid was characterized using FTIR & <sup>13</sup>C-NMR spectra, FESEM, TEM, *etc.*

## Conflicts of interest

There are no conflicts to declare.

## Acknowledgements

SN thanks Vellore Institute of Technology (for providing RGEMS SEED GRANT), and IISER Pune. HDS and PS thank CSIR for a fellowship. VR acknowledge IISER-Pune for the necessary funding. DC thanks DST-Inspire for financial assistance. RK thanks AFOSR under award number FA2386-21-1-4022 for financial support. We acknowledge the SERB (CRG/2021/008250) and MHRD-FAST (MHRD Project 150 (F.No.5-5/2014 TS-VII & F.No. 22-2/2016 TS-II/TC)). We gratefully acknowledge the DST Material for Energy Storage program (DST/TMD/MES/2k17/103), Air Force Office of Scientific Research (AFOSR) under award number FA2386-21-1-4022, MHRD-STARS program (STARS/APR2019/CS/278/FS) and the “DST-Nanomission under the Thematic Unit Program” (EMR/2016/

003553) for the financial support. We acknowledge the National Supercomputing Mission (NSM) for providing computing resources of 'PARAM Brahma' at IISER Pune, which is implemented by C-DAC and supported by the Ministry of Electronics and Information Technology (MeitY) and Department of Science and Technology (DST), Government of India.

## Notes and references

- 1 A. Baughman and E. A. Arens, *ASHRAE Trans.*, 1996, **102**, 192–211.
- 2 D. Bridgeman, J. Corral, A. Quach, X. Xian and E. Forzani, *Langmuir*, 2014, **30**, 10785–10791.
- 3 K. Nagaya, T. Senbongi, Y. Li, J. Zheng and I. Murakami, *Appl. Therm. Eng.*, 2006, **26**, 1545–1551.
- 4 A. Marchetti, S. Pilehvar, L. Hart, D. L. Pernia, O. Voet, W. Anaf, G. Nuyts, E. Otten, S. Demeyer, O. Schalm and K. D. Wael, *Build. Environ.*, 2017, **126**, 132–146.
- 5 A. TenWolde and C. L. Pilon, *Proceedings of Thermal Performance of the Exterior Envelopes of Whole Buildings X*, 2007.
- 6 H. Goderis, G. Ampe, M. Feyten, B. Fouwe, W. Guffens, S. Van Cauwenbergh and P. Tobback, *Biotechnol. Bioeng.*, 1987, **30**, 258–266.
- 7 W. H. Organization, *Air Quality Guidelines: Global Update 2005: Particulate Matter, Ozone, Nitrogen Dioxide, and Sulfur Dioxide*, 2006.
- 8 F. Puppò, A. Dave, M.-A. Doucey, D. Sacchetto, C. Baj-Rossi, Y. Leblebici, G. De Micheli and S. Carrara, *IEEE Trans. NanoBiosci.*, 2014, **13**, 19–30.
- 9 D. Dobrynin, G. Friedman, A. Fridman and A. Starikovskiy, *New J. Phys.*, 2011, **13**, 103033.
- 10 R. Reich and L. Morien, *Appl. Environ. Microbiol.*, 1982, **43**, 609–614.
- 11 L. Monico, A. Chieli, S. De Meyer, M. Cotte, W. de Nolf, G. Falkenberg, K. Janssens, A. Romani and C. Miliani, *Chem. – Eur. J.*, 2018, **24**, 11584–11593.
- 12 K. L. Vikse, M. P. Woods and J. S. McIndoe, *Organometallics*, 2010, **29**, 6615–6618.
- 13 J. A. Mosely, P. Stokes, D. Parker, P. W. Dyer and A. M. Messinis, *Eur. J. Mass Spectrom.*, 2018, **24**, 74–80.
- 14 H. W. Roesky, M. G. Walawalkar and R. Murugavel, *Acc. Chem. Res.*, 2001, **34**, 201–211.
- 15 J. Dai, H. Zhao, X. Lin, S. Liu, Y. Liu, X. Liu, T. Fei and T. Zhang, *ACS Appl. Mater. Interfaces*, 2019, **11**, 6483–6490.
- 16 G. Korotcenkov, *Handbook of Humidity Measurement, Volume 2: Electronic and Electrical Humidity Sensors*, CRC Press, 2019.
- 17 S. Rauf, M. T. Vijjapu, M. A. Andrés, I. Gascón, O. Roubeau, M. Eddaoudi and K. N. Salama, *ACS Appl. Mater. Interfaces*, 2020, **12**, 29999–30006.
- 18 L. Gilmanova, V. Bon, L. Shupletsov, D. Pohl, M. Rauche, E. Brunner and S. Kaskel, *J. Am. Chem. Soc.*, 2021, **143**, 18368–18373.
- 19 S. Jhulki, A. M. Evans, X.-L. Hao, M. W. Cooper, C. H. Feriante, J. Leisen, H. Li, D. Lam, M. C. Hersam, S. Barlow, J.-L. Brédas, W. R. Dichtel and S. R. Marder, *J. Am. Chem. Soc.*, 2020, **142**, 783–791.
- 20 F. Haase and B. V. Lotsch, *Chem. Soc. Rev.*, 2020, **49**, 8469–8500.
- 21 M. S. Lohse and T. Bein, *Adv. Funct. Mater.*, 2018, **28**, 1705553.
- 22 H. Wei, S. Chai, N. Hu, Z. Yang, L. Wei and L. Wang, *Chem. Commun.*, 2015, **51**, 12178–12181.
- 23 Y. Zeng, R. Zou and Y. Zhao, *Adv. Mater.*, 2016, **28**, 2855–2873.
- 24 N. Huang, R. Krishna and D. Jiang, *J. Am. Chem. Soc.*, 2015, **137**, 7079–7082.
- 25 A. Esrafil, A. Wagner, S. Inamdar and A. P. Acharya, *Adv. Healthcare Mater.*, 2021, **10**, 2002090.
- 26 C. R. Mulzer, L. Shen, R. P. Bisbey, J. R. McKone, N. Zhang, H. c. D. Abruña and W. R. Dichtel, *ACS Cent. Sci.*, 2016, **2**, 667–673.
- 27 R. Kushwaha, S. Haldar, P. Shekhar, A. Krishnan, J. Saha, P. Hui, C. P. Vinod, C. Subramaniam and R. Vaidhyanathan, *Adv. Energy Mater.*, 2021, **11**, 2003626.
- 28 S. Kandambeth, V. S. Kale, O. Shekhah, H. N. Alshareef and M. Eddaoudi, *Adv. Energy Mater.*, 2022, **12**, 2100177.
- 29 Z. Tian, V. S. Kale, Y. Wang, S. Kandambeth, J. Czaban-Jozwiak, O. Shekhah, M. Eddaoudi and H. N. Alshareef, *J. Am. Chem. Soc.*, 2021, **143**, 19178–19186.
- 30 Y. Li, W. Chen, R. Gao, Z. Zhao, T. Zhang, G. Xing and L. Chen, *Chem. Commun.*, 2019, **55**, 14538–14541.
- 31 Y. Zhi, Z. Wang, H. L. Zhang and Q. Zhang, *Small*, 2020, **16**, 2001070.
- 32 J. Guo and D. Jiang, *ACS Cent. Sci.*, 2020, **6**, 869–879.
- 33 D. Mullangi, D. Chakraborty, A. Pradeep, V. Koshti, C. P. Vinod, S. Panja, S. Nair and R. Vaidhyanathan, *Small*, 2018, **14**, 1801233.
- 34 D. Chakraborty, P. Shekhar, H. D. Singh, R. Kushwaha, C. Vinod and R. Vaidhyanathan, *Chem. – Asian J.*, 2019, **14**, 4767–4773.
- 35 D. Chakraborty, S. Nandi, D. Mullangi, S. Haldar, C. P. Vinod and R. Vaidhyanathan, *ACS Appl. Mater. Interfaces*, 2019, **11**, 15670–15679.
- 36 C. Chandran, H. D. Singh, L. S. Leo, P. Shekhar, D. Rase, D. Chakraborty, C. P. Vinod and R. Vaidhyanathan, *J. Mater. Chem. A*, 2022, **10**, 15647–15656.
- 37 L. Stegbauer, K. Schwinghammer and B. V. Lotsch, *Chem. Sci.*, 2014, **5**, 2789–2793.
- 38 K. Gottschling, G. k. Savasci, H. Vignolo-González, S. Schmidt, P. Mauker, T. Banerjee, P. Rovó, C. Ochsensfeld and B. V. Lotsch, *J. Am. Chem. Soc.*, 2020, **142**, 12146–12156.
- 39 S. Wan, J. Guo, J. Kim, H. Ihee and D. Jiang, *Angew. Chem., Int. Ed.*, 2009, **48**, 5439–5442.
- 40 E. Jin, J. Li, K. Geng, Q. Jiang, H. Xu, Q. Xu and D. Jiang, *Nat. Commun.*, 2018, **9**, 1–10.
- 41 S. Haldar, D. Chakraborty, B. Roy, G. Banappanavar, K. Rinku, D. Mullangi, P. Hazra, D. Kabra and R. Vaidhyanathan, *J. Am. Chem. Soc.*, 2018, **140**, 13367–13374.
- 42 P. Das, G. Chakraborty, S. Tyagi and S. K. Mandal, *ACS Appl. Mater. Interfaces*, 2020, **12**, 52527–52537.



- 43 X. Liu, D. Huang, C. Lai, G. Zeng, L. Qin, H. Wang, H. Yi, B. Li, S. Liu and M. Zhang, *Chem. Soc. Rev.*, 2019, **48**, 5266–5302.
- 44 A. F. EL-Mahdy, A. M. Elewa, S. W. Huang, H. H. Chou and S. W. Kuo, *Adv. Opt. Mater.*, 2020, **8**, 2000641.
- 45 L. Ascherl, E. W. Evans, J. Gorman, S. Orsborne, D. Bessinger, T. Bein, R. H. Friend and F. Auras, *J. Am. Chem. Soc.*, 2019, **141**, 15693–15699.
- 46 G. Das, B. P. Biswal, S. Kandambeth, V. Venkatesh, G. Kaur, M. Addicoat, T. Heine, S. Verma and R. Banerjee, *Chem. Sci.*, 2015, **6**, 3931–3939.
- 47 P. Albacete, A. López-Moreno, S. Mena-Hernando, A. E. Platero-Prats, E. M. Pérez and F. Zamora, *Chem. Commun.*, 2019, **55**, 1382–1385.
- 48 H.-L. Qian, C. Dai, C.-X. Yang and X.-P. Yan, *ACS Appl. Mater. Interfaces*, 2017, **9**, 24999–25005.
- 49 L. Ascherl, E. W. Evans, M. Hennemann, D. Di Nuzzo, A. G. Hufnagel, M. Beetz, R. H. Friend, T. Clark, T. Bein and F. Auras, *Nat. Commun.*, 2018, **9**, 1–8.
- 50 A. F. El-Mahdy, M.-Y. Lai and S.-W. Kuo, *J. Mater. Chem. C*, 2020, **8**, 9520–9528.
- 51 P. Wang, F. Zhou, C. Zhang, S.-Y. Yin, L. Teng, L. Chen, X.-X. Hu, H.-W. Liu, X. Yin and X.-B. Zhang, *Chem. Sci.*, 2018, **9**, 8402–8408.
- 52 L. Chen, L. He, F. Ma, W. Liu, Y. Wang, M. A. Silver, L. Chen, L. Zhu, D. Gui and J. Diwu, *ACS Appl. Mater. Interfaces*, 2018, **10**, 15364–15368.
- 53 Y. Zhang, X. Shen, X. Feng, H. Xia, Y. Mu and X. Liu, *Chem. Commun.*, 2016, **52**, 11088–11091.
- 54 S. Jhulki, A. M. Evans, X.-L. Hao, M. W. Cooper, C. H. Feriante, J. Leisen, H. Li, D. Lam, M. C. Hersam and S. Barlow, *J. Am. Chem. Soc.*, 2020, **142**, 783–791.
- 55 Y. Zhang, W. Zhang, Q. Li, C. Chen and Z. Zhang, *Sens. Actuators, B*, 2020, **324**, 128733.
- 56 H. Singh, V. K. Tomer, N. Jena, I. Bala, N. Sharma, D. Nepak, A. D. Sarkar, K. Kailasam and S. K. Pal, *J. Mater. Chem. A*, 2017, **5**, 21820–21827.
- 57 S. Nandi, S. K. Singh, D. Mullangi, R. Illathvalappil, L. George, C. P. Vinod, S. Kurungot and R. Vaidhyanathan, *Adv. Energy Mater.*, 2016, **6**, 1601189.
- 58 D. Mullangi, V. Dhavale, S. Shalini, S. Nandi, S. Collins, T. Woo, S. Kurungot and R. Vaidhyanathan, *Adv. Energy Mater.*, 2016, **6**, 1600110.
- 59 S. Haldar, K. Roy, S. Nandi, D. Chakraborty, D. Puthusseri, Y. Gawli, S. Ogale and R. Vaidhyanathan, *Adv. Energy Mater.*, 2018, **8**, 1702170.
- 60 M. Frisch, G. Trucks, H. Schlegel, G. Scuseria, M. Robb, J. Cheeseman, G. Scalmani, V. Barone, B. Mennucci and G. Petersson, *Gaussian*, Wallingford, 2009.
- 61 N. Sun, Y. Jin, H. Wang, B. Yu, R. Wang, H. Wu, W. Zhou and J. Jiang, *Chem. Mater.*, 2022, **34**, 1956–1964.
- 62 R. Maity, D. Chakraborty, S. Nandi, A. K. Yadav, D. Mullangi, C. Vinod and R. Vaidhyanathan, *ACS Appl. Nano Mater.*, 2019, **2**, 5169–5178.